JGR Solid Earth

RESEARCH ARTICLE
10.1029/2022JB026201

Evolution of Stresses Over Conjugate Faults in Hjalli-Ölfus, South Iceland

Revathy M. Parameswaran[1,2], Ingi Th. Bjarnason[1,3], and Bergthóra S. Thorbjarnardóttir[1]

[1]Institute of Earth Sciences, University of Iceland, Reykjavik, Iceland, [2]Now at Geophysical Institute, University of Alaska Fairbanks, Fairbanks, AK, USA, [3]Nordvulc Volcanological Centre, Institute of Earth Sciences, University of Iceland, Reykjavik, Iceland

Key Points:

- Hjalli-Ölfus predominantly hosts oblique-normal and left-lateral strike-slip earthquakes on faults that orient in ~ENE-WSW directions
- Stress-changes due to the Hengill inflation and seismicity are reflected as rotations in the maximum horizontal stress (SHmax) orientations
- The state of stress in Hjalli-Ölfus mimics that of the Reykjanes Peninsula during interseismic periods

Supporting Information:

Supporting Information may be found in the online version of this article.

Correspondence to:

R. M. Parameswaran,
rmparameswaran@alaska.edu

Citation:

Parameswaran, R. M., Bjarnason, I. T., & Thorbjarnardóttir, B. S. (2023). Evolution of stresses over conjugate faults in Hjalli-Ölfus, South Iceland. *Journal of Geophysical Research: Solid Earth*, *128*, e2022JB026201. https://doi.org/10.1029/2022JB026201

Received 5 DEC 2022
Accepted 7 MAR 2023

Author Contributions:

Conceptualization: Revathy M. Parameswaran, Ingi Th. Bjarnason
Data curation: Revathy M. Parameswaran, Bergthóra S. Thorbjarnardóttir
Formal analysis: Revathy M. Parameswaran
Funding acquisition: Ingi Th. Bjarnason
Investigation: Revathy M. Parameswaran
Methodology: Revathy M. Parameswaran, Ingi Th. Bjarnason
Project Administration: Ingi Th. Bjarnason
Supervision: Ingi Th. Bjarnason
Validation: Revathy M. Parameswaran

Abstract Hjalli-Ölfus is the westernmost segment of the east-west transform South Iceland Seismic Zone (SISZ), which is the eastward extension of the ~ENE-trending transtensional Reykjanes Peninsula (RP). Historically, the area has shown an interactive behavior with the Hengill volcanic system to the north and the central SISZ to the east. We analyzed the state of stress and faulting mechanisms in Hjalli-Ölfus between July 1991 and December 1999, in connection with the Hengill inflation episode (Feigl et al., 2000, https://doi.org/10.1029/2000JB900209) and the 13th November 1998 Mw 5.1 Hjalli-Ölfus earthquake. We find that this region predominantly hosted oblique-normal and left-lateral strike-slip events (4–10 km-depth), with most nodal planes oriented along ~ENE or ~WSW directions (75° ± 15° or 255° ± 15°). We identify 5 stages of stress evolution from January 1991 to December 1999 over which Hjalli-Ölfus experiences both spatial and temporal shifts in stress-states. The Hengill inflation likely loaded both the fissure zone and western Ölfus, culminating in the Mw 5.4 (Hengill) and Mw 5.1 (Hjalli-Ölfus) earthquakes. Following these events, the maximum compressive stress (SHmax) orientation near the location of the Mw 5.1 earthquake showed a ~5°–7° counterclockwise swing, compared to SHmax before June 1998. The average SHmax (~40° ± 1°) and minimum principal stress (σ_3 ~ 130° ± 1°) are comparable to geological trends in the RP. We conclude that Hjalli-Ölfus shows clockwise SHmax rotation upon loading, while a stress-drop reverses the rotation. We also posit that the region, especially the western end, behaves like the RP during interseismic periods.

Plain Language Summary Iceland hosts a predominantly rifting plate boundary that is offset by two ~east-west trending, horizontally sliding (transform-faulting) segments, one in the north and the other in the south. The southern segment, known as the South Iceland Seismic Zone (SISZ), is seismically productive and is flanked by diverging volcanic arms. The SISZ has hosted several moderate to large earthquakes on north-south faults that cut across it. However, the westernmost end of the SISZ, also known as Hjalli-Ölfus, differs from the rest of the SISZ as it seems to host earthquakes in an ~east-northeast direction, similar to its western, rifting neighbor, namely, the Reykjanes Peninsula. The activity in Hjalli-Ölfus also seems to be responsive to volcanic/magmatic activity in the Hengill volcano to its north. This suggests the existence of multiple stress fields—volcanic, tectonic, or both—acting on the Hjalli-Ölfus segment. Here, we study earthquakes in Hjalli-Ölfus from January 1991 to December 1999, including a magnitude 5.1 earthquake in November 1998, to identify possible stress changes along the segment over time. Results indicate that magmatic deformation and seismic activity near the Hengill volcano directly influence the seismic productivity of Hjalli-Ölfus, and that this seismicity is similar to that of the Reykjanes Peninsula.

1. Introduction

Seismic zones adjacent to one or more tectonically active regions are subject to fluctuating states of stress. These changes in stress fields are best reflected in the associated seismicity and crustal deformation. The South Iceland Seismic Zone (SISZ), a left-lateral transform segment of an overall diverging plate boundary in Iceland, is a fitting example of such a system. The SISZ lies sandwiched between the transtensional Reykjanes Peninsula (RP) in the west and the diverging Eastern Volcanic Zone (EVZ) in the east (Einarsson et al., 1981) (Figure 1a). North-northwest of the SISZ lies the Western Volcanic Zone (WVZ) that runs parallel to the EVZ, and spreads at one-third to half the rate of its eastern counterpart (Árnadóttir et al., 2008; Gudmundsson, 2007; Perlt & Heinert, 2006). The southern end of the WVZ hosts the Hengill volcanic system that has witnessed notable inflation-deflation episodes over recent decades (Ducrocq et al., 2021; Feigl et al., 2000; Sigmundsson et al., 1997). The active central volcanic system, Hengill, lies north of the western part of the SISZ (regionally

Visualization: Revathy M. Parameswaran
Writing – original draft: Revathy M. Parameswaran
Writing – review & editing: Revathy M. Parameswaran, Ingi Th. Bjarnason, Bergthóra S. Thorbjarnardóttir

known as Ölfus), with its fissure swarms extending into western Ölfus. Therefore, western SISZ is optimally placed to experience shifts in its stress regime influenced by its neighbors—Hengill and the RP.

The SISZ hosts N-S right-lateral faults stacked in a "bookshelf"-like pattern (Erlendsson & Einarsson, 1996), stitching across a cumulative E-W left-lateral movement (Einarsson et al., 1981). The plate motion here is accommodated by release of seismic moment along the N-S faults (Einarsson et al., 1981; Roth, 2004). One notable exception to this trend is seen west of the river Ölfusá in the Ölfus region where seismicity trends mostly ENE-WSW (Figures 1b and 2a) (e.g., Parameswaran et al., 2020). Furthermore, given its proximity to the Hengill volcanic system in the north, this section of SISZ also exhibits an interactive seismic pattern with Hengill (e.g., Feigl et al., 2000) (Figure 2b). This interaction was best observed in modern times following the 4 June 1998 Mw 5.4 Hengill earthquake, after which a Mw 5.1 earthquake occurred in western Ölfus, (Hjalli-Ölfus, following Parameswaran et al., 2020) on 13 November 1998 (Lund & Bödvarsson, 2002; Lund & Slunga, 1999; Parameswaran et al., 2020; Rögnvaldsson, Arnadóttir, et al., 1998; Rögnvaldsson, Gudmundsson, et al., 1998; Vogfjörd et al., 2005). Thus far, there is no study that analyses the evolution of the stress field across western Ölfus leading up to the November 1998 earthquake. This is of importance because, post-instrumentation, the Ölfus region has shown interactions with neighboring zones resulting in high earthquake hazard (see Supporting Material from Parameswaran et al., 2020). The sensitivity of Ölfus, especially its western segment Hjalli-Ölfus, to activity in neighboring zones allows for the study of stress field interaction on a much shorter timescale than is normally possible in South Iceland. Hjalli-Ölfus is located to the east of a seismic gap (locked zone) on the RP, approximately between Bláfjöll and Brennisteinsfjöll (https://icelandicvolcanos.is). This zone poses the greatest earthquake hazard to the capitol region. Therefore, a better understanding of a possible interaction between this gap, and stress changes in the Hengill and Hjalli-Ölfus regions is important.

1.1. Seismotectonic Background and Relevance of the Study

The strain release through large South Iceland earthquakes along the N-S features on the SISZ often result in rupture lengths of 20 km or greater, although the annual microseismicity here spans a ∼10–20-km-wide zone, (Bjarnason, Cowie, et al., 1993; Björnsson, 1976; Einarsson et al., 1981; Roth, 2004). In recent times, two large earthquake sequences in the years 2000 (17 June Mw 6.5 and 21 June Mw 6.4) (Árnadóttir et al., 2001; Stefánsson et al., 2000) and 2008 (29 May; two ∼M6 events in a span of 3s) (Hensch et al., 2016) have occurred in the SISZ, all on ∼N-S faults (Figure 1b; Table S1 in Supporting Information S1). Meanwhile, in the RP, the left-lateral shear is accommodated by right-lateral ∼N-S faults, ∼N40°E extensional faulting, and occasional left-lateral deformation (Árnadóttir et al., 2006; Clifton & Schlische, 2003; Keiding et al., 2008, 2009; Khodayar et al., 2018). However, most of the plate-motion related strain release and larger earthquakes ($M \sim 6.0$) occur along the right-lateral N-S faults in the east RP (Árnadóttir et al., 2004; Björnsson, 1976; Erlendsson and Einarsson, 1996). However, this does not preclude the occurrence of seismicity in the ENE-WSW direction along the RP, as noted by some authors (e.g., Figure 2 in Geoffroy & Dorbath, 2008). This ENE-WSW direction became more prominent recently with heightened seismicity and crustal deformation in western/central RP, starting in 2020 near Mt. Thorbjörn eventually leading to the prolonged effusive fissure eruptions in Fagradalsfjall in 2021 (e.g., Flóvenz et al., 2022). The variations in faulting styles, focal mechanisms, earthquake magnitudes, and seismic intervals in the RP point toward varying stress-fields over the E-W length of the peninsula (Keiding et al., 2009). By extension, we examine possible spatio-temporal stress variations in the SISZ due to its close proximity and similarity to the seismotectonics of the RP.

In a preceding work, we relocated earthquakes that occurred between July 1991 and December 1999, including the seismic sequence following the June 1998 Mw 5.4 Hengill and November 1998 Mw 5.1 Hjalli-Ölfus earthquake (Parameswaran et al., 2020). The foreshock activity for the Hjalli-Ölfus mainshock was found to shift from a N-S trend to a ∼ENE trend ∼24 hr prior to the event. Subsequently, ∼84% of the aftershocks aligned in the ∼ENE direction and the rest along a ∼N-S trend. We found that the seismicity in Hjalli-Ölfus between July 1991 and December 1999 was largely limited to 4–8 km depth range. The main trend of seismicity and faulting was found to have an unusual ∼N75°E trend compared to the general ∼N-S faulting and seismicity along the rest of the SISZ. The seismicity triggered in Hjalli-Ölfus following the east-Ölfus ∼M6 doublet earthquakes in 2008 also maintained a stark ∼ENE-WSW seismic trend (Brandsdóttir et al., 2010).

As observed in 2008, Hjalli-Ölfus has shown sensitivity to seismicity in central/western SISZ (Brandsdóttir et al., 2010; Hreinsdóttir et al., 2009), plate spreading (Árnadóttir et al., 2018), and inflation/contraction in the

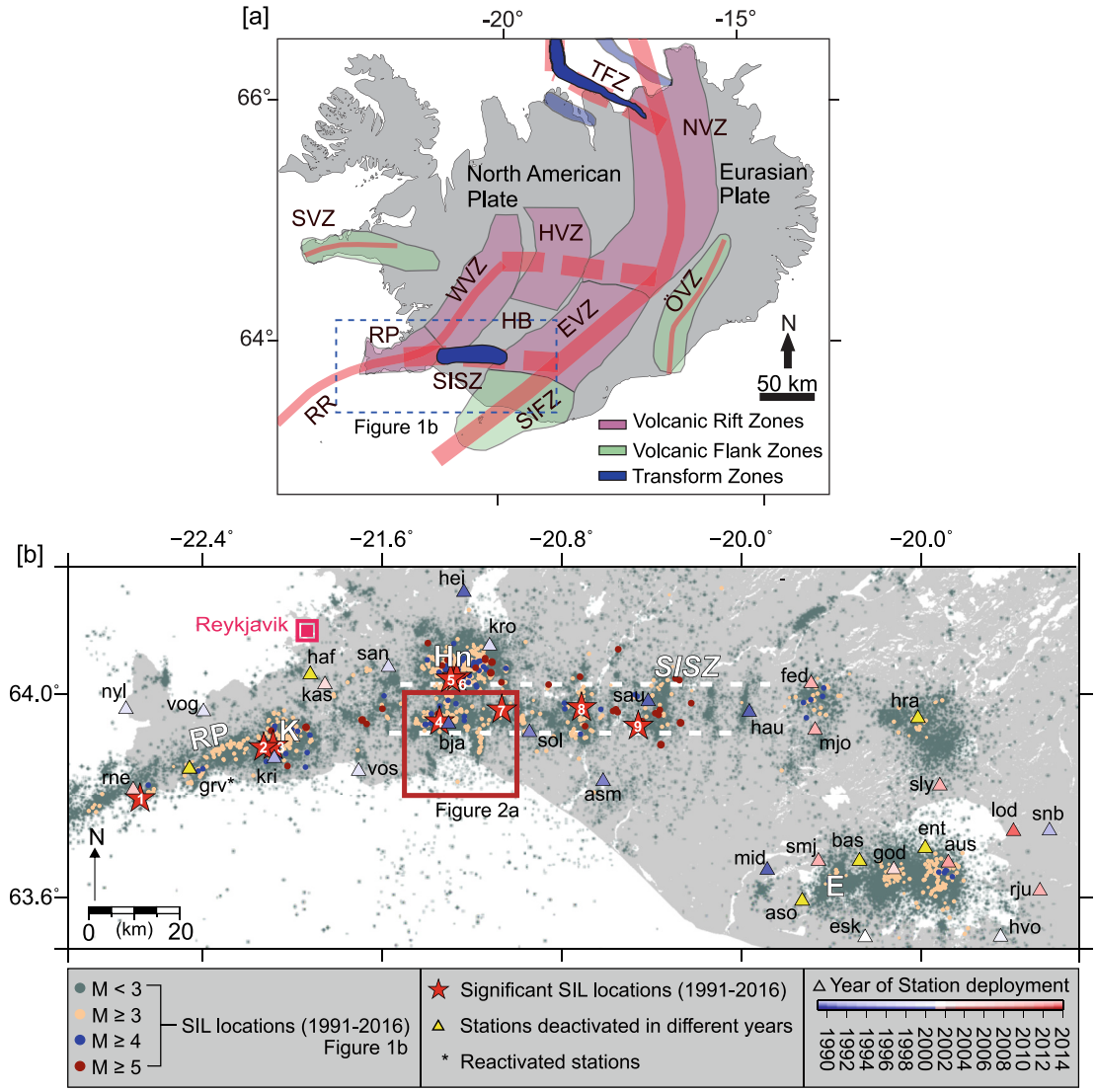

Figure 1. Tectonic and seismic setting of South Iceland: (a) Prominent tectonic and volcanic regions in Iceland. TFZ, Tjörnes Fracture Zone; NVZ, Northern Volcanic Zone; EVZ, Eastern Volcanic Zone; ÖVZ, Öræfajökull Volcanic Zone; HVZ, Hofsjökull Volcanic Zone; WVZ, Western Volcanic Zone; SVZ, Snæfellsnes Volcanic Zone; RP, Reykjanes Peninsula; RR, Reykjanes Ridge; SISZ, South-Iceland Seismic Zone; SIFZ, South-Iceland Volcanic Flank Zone; HB, Hreppar Block; Hn, Hengill; K, Krysuvík; E, Eyjafjallajökull (modified after Sigmundsson et al., 2018). (b) Seismicity in south/southwest Iceland between 1991 and 2016, recorded by the South Iceland Lowlands network as mapped out in the figure. Numbers marked in white represent significant earthquakes in the region, (tabulated in Table S1 of the Supporting Information S1). The station colors (blue-to-red scale) represent the years of deployment for stations that are still active, while yellow shows those that have since been deactivated.

Hengill volcanic system (Feigl et al., 2000; Rögnvaldsson, Arnadóttir, et al., 1998; Sigmundsson et al., 1997). The seismicity here has been continuously recorded by the Icelandic Meteorological Office (IMO) seismic network (initially established as the South Iceland Lowlands or SIL network) from 1991 to the present (e.g., Bödvarsson et al., 1996; Jakobsdóttir, 2008; Stefánsson, 2011). We select the time interval from July 1991 to December 1999 to analyze the spatio-temporal variations in stresses in Hjalli-Ölfus for the following reasons—(a) there is documented evidence of stress-change surrounding the 13 November 1998 earthquake (Lund & Bödvarsson, 2002) following the 1993–1998 inflation episode in Hengill (Feigl et al., 2000); (b) the aftershock sequence in Hjalli-Ölfus following the 2008 ~M6 doublet in eastern Ölfus exhibited pre- and post-seismic rotation of the maximum horizontal stress (Hensch et al., 2016); (c) geodetic estimates of pre-seismic strain based on GPS data from 2001 to 2015 in Ölfus show a decrease in normal stresses on N-S faults before the 29 May 2008 earthquakes due to contraction in the Hengill area, followed by an apparent increase in shear strain with time (Árnadóttir et al., 2018). A spatio-temporal investigation of stress-variations in Ölfus would yield some clarity

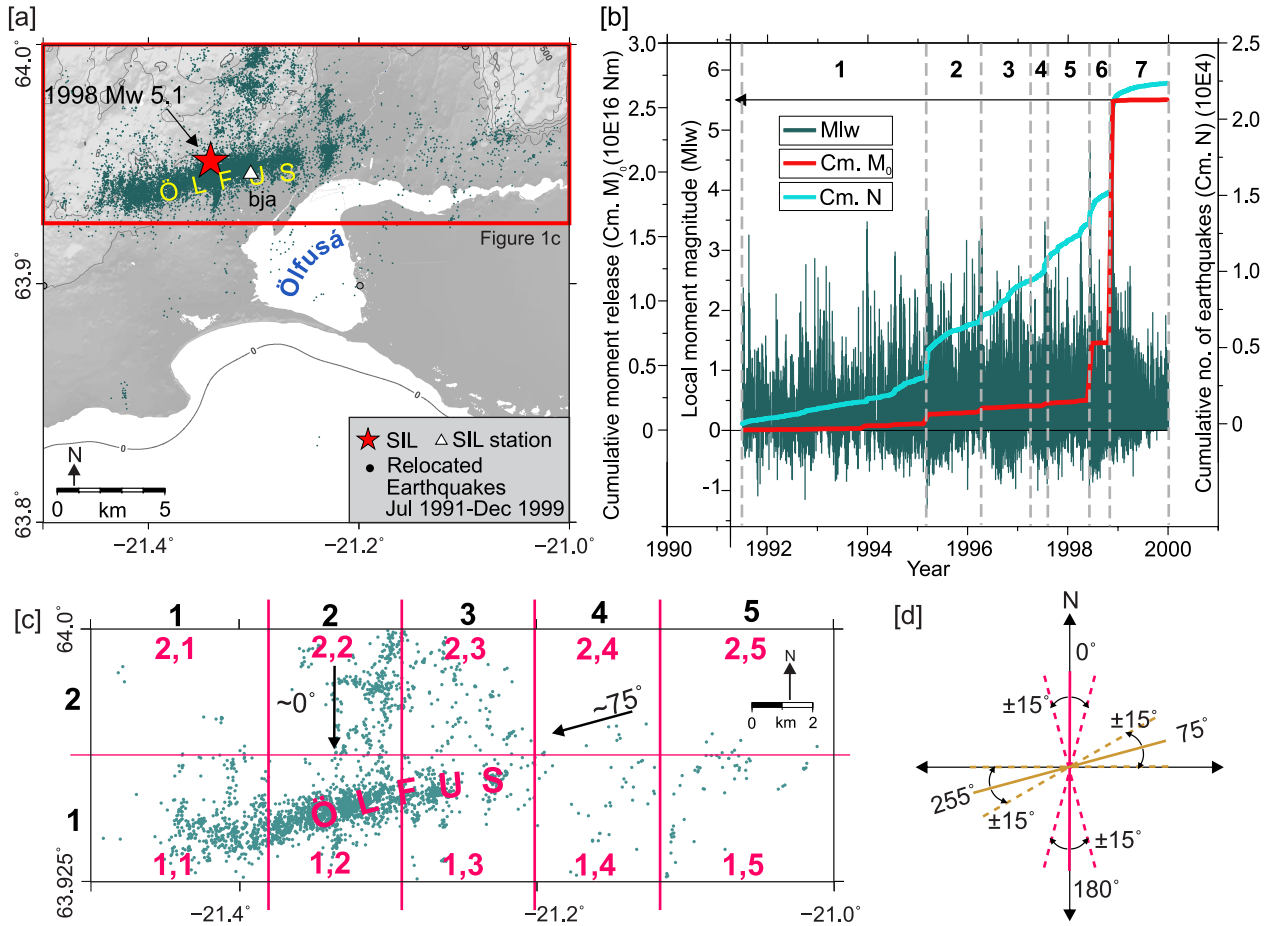

Figure 2. Spatio-temporal divisions of Hjalli-Ölfus seismicity from July 1991–December 1999: (a) relocated events from July 1991 to December 1999 in the Ölfus study area, including the 13 November 1998 Mw 5.1 Ölfus earthquake. (b) Cumulative number of all events and moment release in Ölfus over the prescribed time period. (c) Grid division for the Hjalli-Ölfus region defined by red box in (a). Events plotted in the figure are relocated events selected based on panel (d) and the selection criteria described in Section 2.2. (d) Prominent seismic trends in Hjalli-Ölfus (N-S and ENE-WSW) (after Parameswaran et al., 2020), used for event selection. Events with strike angles within N75°E ± 15°, S75°W ± 15°, N ± 15°, S ± 15° are selected for further analysis.

on the activity in the region, the factors affecting it, and the implications this could have on potential interactions with neighboring volcano-tectonic systems.

2. Data and Methodology

2.1. Data

We procured data associated with 22,354 earthquakes from the Hjalli-Ölfus region (63.8°–64°N and 21.0°–21.5°W) between July 1991 and December 1999 from IMO (IMO, 2017). These were originally recorded and located using the 1-D SIL velocity model (Stefánsson et al., 1993) based on refraction profiles in western/southwestern Iceland (Bjarnason, Menke, et al., 1993). Of these earthquakes, we employed relocated events obtained from our previous work (Parameswaran et al., 2020) to compute stress changes in the study area (Figure 1b). For consistency, we used the same seven time-windows (*TWs*) as in Parameswaran et al. (2020)—*(1) July 1991–February 1995 (3,086 earthquakes), (2) March 1995–March 1996 (3,699 earthquakes), (3) April 1996–March 1997 (2,623 earthquakes), (4) April 1997–July 1997 (1,396 earthquakes), (5) August 1997–May 1998 (2,335 earthquakes), (6) June 1998–October 1998 (2,057 earthquakes), and (7) November 1998–December 1999 (7,158 earthquakes)* (Figures 2a and 2b). The relocations were performed using constant-velocity layers based on the SIL model, but with twice as many layers as the gradient version, and data from active seismic stations (12 stations in *TW1*, 12 in *TW2*, 20 in *TW3*, 23 in *TW4*, 22 in *TW5*, 23 in *TW6*, and 25 in *TW7*) (Parameswaran et al., 2020).

2.2. Grid Definition and Data Selection

The relocated Ölfus earthquakes from July 1991 to December 1999 were mostly confined to a narrow ~ENE-WSW trending zone in Hjalli-Ölfus (Parameswaran et al., 2020). Based on the spatial spread of these relocated events over the seven *TWs*, Hjalli-Ölfus is divided into 5 (east-west) × 2 (north-south) grids (Figure 2c; Figure S1 in Supporting Information S1). The seismic relocations also indicate that most of the Hjalli-Ölfus seismicity is at depths of 4–10 km, with the highest concentration of events within 4 to 6 km-depths (Parameswaran et al., 2020) (Figure S2 in Supporting Information S1). Shallower events in this region are largely localized to faults lying north toward the Hengill fissure zone (see Parameswaran et al., 2020). Therefore, this study focuses on events within seismogenic depths of 4–10 km. The fault plane solutions (FPSs) corresponding to the relocated events were directly obtained from the IMO database of routinely analyzed earthquakes. These were calculated using an amplitude spectral method based on Slunga (1981) and Rögnvaldsson and Slunga (1993), where the entire parameter space of strike, dip, and rake is searched for each earthquake, and the nodal planes that best satisfy polarity observations and amplitude spectra of compressional and shear waves are chosen. A statistical test is applied to evaluate the significance of a double-couple solution for the earthquake source (Slunga, 1981). Rögnvaldsson and Slunga (1993) assessed the accuracy of the IMO network in determining the orientation of the earthquake sources by adding noise to synthetic seismograms. Accuracy depends on the data coverage, that is, the number of observations (polarities and amplitude spectra), and the network distribution. The network distribution for the location of Hjalli-Ölfus earthquakes is similar or better than the synthetic network of Rögnvaldsson and Slunga (1993). By comparing the number of observations used in the synthetic tests (Table 3 in Rögnvaldsson & Slunga, 1993) with the of number of observations (phases amplitudes and polarities) that the selected FPSs were constructed from (Figure S3 in Supporting Information S1), we conclude that ~90% of the total selected FPSs for the present study have uncertainty in orientations of earthquake sources within 15°, and ~70% within 5°. Parameswaran et al. (2020) show that the absolute error for nearly half the data in the SIL catalog for Hjalli-Ölfus is ~±1 km, while the relative error is an order of magnitude lesser. The standard deviations (SDs) of uncertainties in the latitude and longitude of the relocated events for all TWs are ≤0.6 km (Supporting Figures S1–S7 in Parameswaran et al., 2020), whereas the SDs in depth are ≤1 km (Supporting Figures S1–S7 in Parameswaran et al., 2020). Meanwhile, the spatial distribution of the SIL network between 1991 and 1999 was greater by over an order of magnitude (Figure 1b). That suggests that spatial and temporal changes in FPSs and stress field may be resolvable with similar accuracy, especially changes in mean values.

Of the relocated events, we chose FPSs determined using ≥12 P and S amplitudes and ≥4 first polarities (Figure S3 in Supporting Information S1). Further, we narrowed this selection down to events that have FPSs that align with the two primary trends of Hjalli-Ölfus seismicity—(a) averaging at 0° or 180° azimuth, and (b), averaging at 75° or 255° azimuth (Figure 2d). FPSs with strikes within ±15° of these angles were selected for subsequent analysis and will henceforth be referred to as *selected events* (Note: implies "*selected relocated events*"), and the rest are referred to as *non-selected events*. The *selected events* were then subjected to rake analysis and focal mechanism classification (see Section 2.3), followed by stress-inversion (see Section 2.4) over individual grids.

2.3. Rake Analysis and Focal Mechanism Classification

Fault-types can be classified into dip-slip (reverse and normal) and strike-slip (left-lateral and right-lateral) based on both geology and FPSs (Aki & Richards, 1980; Rickard, 1972). Following these conventions, we classified the *selected events* into 8 categories based on rake values, as listed in Supporting Information S1 (Table S2) (e.g., Waite & Smith, 2004; White et al., 2009). This division has been performed on both fault planes of the *selected events* to compare their relative abundance in Hjalli-Ölfus over the defined *TWs* (Planes-a and -b in Figures 3 and 4, and Figures S4–S6 in Supporting Information S1). For completeness, we have also performed a rake analysis on events that do not align with the prominent seismic trend in Hjalli-Ölfus, and these are plotted in Supporting Information S1 (Figure S7). The analysis for *TW1* is depicted in Supporting Information S1 (Figure S4), as the SIL network was in its nascent state during this time, and therefore the data is not well-constrained for stress inversion, despite their relevance in identifying regions of seismic productivity. Besides the rake-analysis, Focal Mechanisms Classification (Álvarez-Gómez, 2019), a python-based tool, was modified and used to generate Ternary plots showing the classification of focal mechanisms and their depth distribution in Hjalli-Ölfus (Figures 3 and 4, and Figures S4–S6 in Supporting Information S1). In Figure S8 in Supporting Information S1 (*TWs 2–7*), we compare strike versus rake angle of the *selected events* to clarify the sense of motion on ~N-S and ~ENE-WSW striking nodal planes (*TW1* in Figure S4 of the Supporting Information S1).

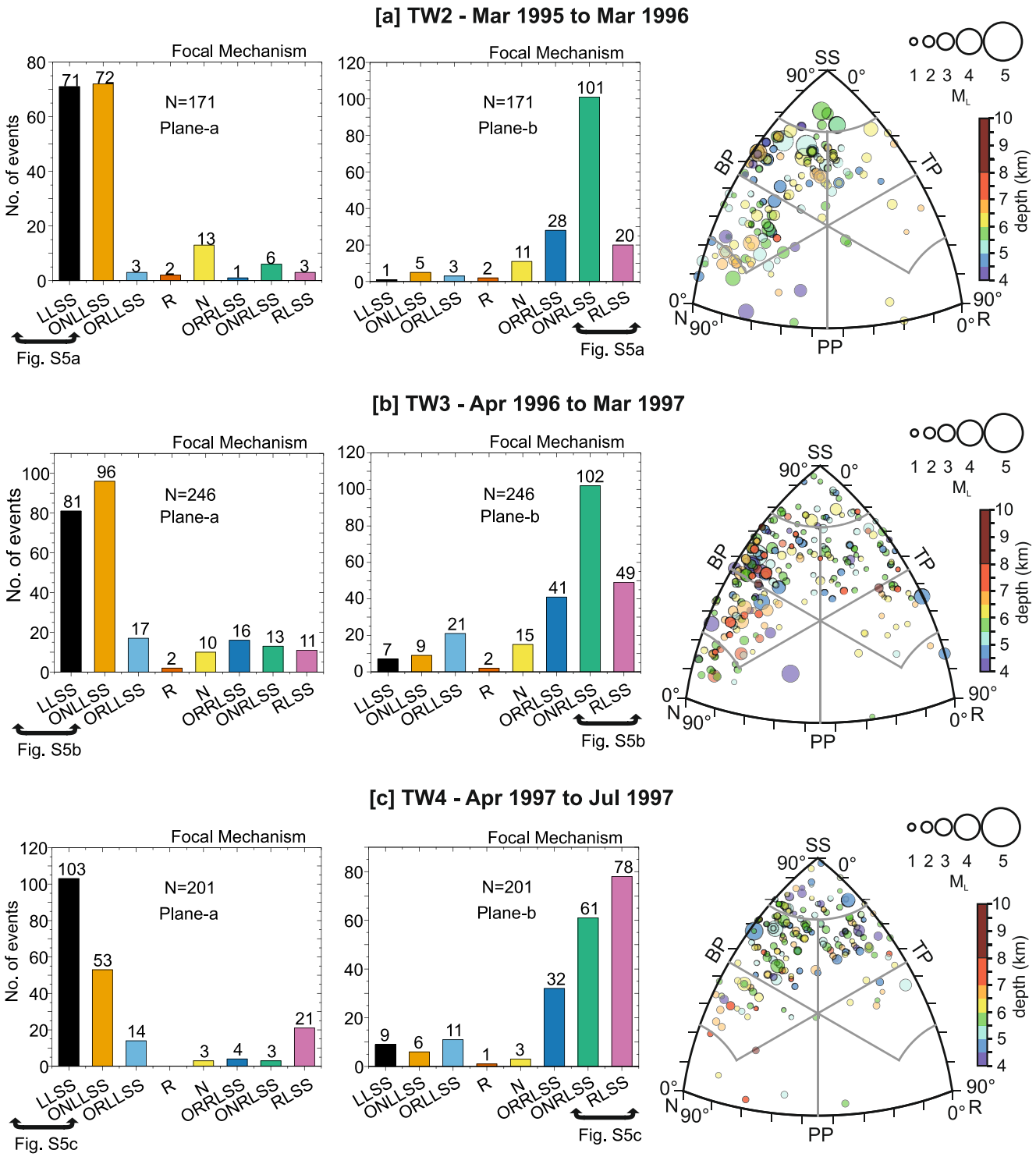

Figure 3. Rake and focal mechanism analysis of selected events for TWs 2, 3, and 4: Bar diagrams depict rake-based classification (see Table S2 in Supporting Information S1) of planes-a and -b of selected events within seismogenic depths of 4–10 km. The ternary plot on the right illustrates the depth and magnitude distribution of all selected events for the corresponding TWs. The ternary plots for major faulting styles are shown in Figure S5 of the Supporting Information S1. (a) *TW2*—March 1995–March 1996, (b) *TW3*—April 1996–March 1997. (c) *TW4*—April 1997–July 1997. BP, TP, and PP stand for B-, T-, and P-axes plunges. R, Reverse; N, Normal; SS, Strike-slip.

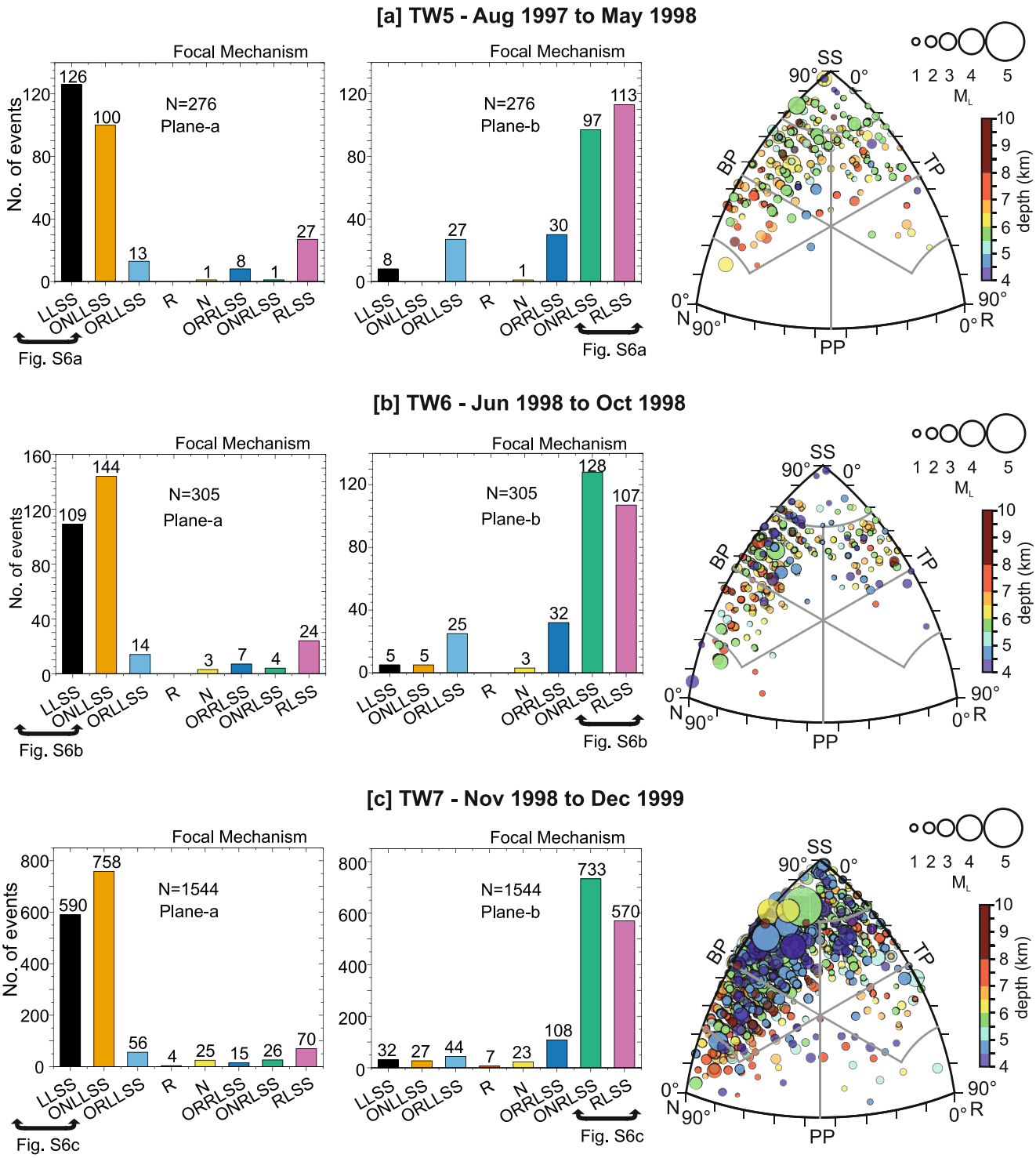

Figure 4. Rake and focal mechanism analysis of selected events for TWs 4 and 5: Bar diagrams and ternary plots are as described in Figure 2. The ternary plots for major faulting styles are shown in Supporting Information S1 (Figure S6). (a) *TW5*—August 1997–May 1998, (b) *TW6*—June 1998–October 1998, (c) *TW7*—November 1998–December 1999. Abbreviations as in Figure 3.

2.4. Stress Inversion

The stress inversions were carried out using the MATLAB-based routine, MSATSI (Martínez-Garzón et al., 2014) that generates a single stress tensor for a chosen set of FPSs. The code is the MATLAB version of the SATSI

routine by Hardebeck and Michael (2006) that follows stress inversion detailed by Michael (1984). The routine also incorporates maximum horizontal stress (SHmax) computation as described by Lund and Townend (2007). The inversion provides the orientations of the three principal stress axes, σ_1 (most compressive), σ_2 (intermediate), and σ_3 (least compressive), and computes the relative stress magnitude, R, that quantifies the relative closeness of σ_2 to σ_1 and σ_3 (Lund & Townend, 2007)

$$R = \frac{\sigma_1 - \sigma_2}{\sigma_1 - \sigma_3} \quad (1)$$

In this study, the Hjalli-Ölfus region is divided into grids as described in Section 2.2. For each grid, a minimum number of 20 events is set to conduct a well-constrained stress inversion. The routine employs bootstrap sampling such that the number of iterations is set to approximately 20 times the number of events selected (Efron & Tibshirani, 1986). In this study, the original data is bootstrap sampled through 2,000 iterations since each *TW* has >100 events. The confidence level for the inversion is set to 95%. Stress inversions are allowed to randomly choose between the nodal planes to resolve any ambiguity in the preferred fault plane, whether N-S ± 15° or ENE-WSW ± 15°—the two, dominant seismic lineations in the region (Figures 5 and 6; Figure S9 in Supporting Information S1). Additionally, another set of inversions was performed for completeness and comparison, now using FPSs of all strike orientations (Figures S10 and S11 in Supporting Information S1). The time windows *TWs 6* and *7* contain two moderately large earthquakes in Hengill (Mw 5.4; 4 June 1998) and Ölfus (Mw 5.1; 13 November 1998), respectively, with considerable aftershock activity in Hengill and Ölfus. Therefore, we inverted for stresses over 4 resolved *TWs* (20 events minimum per grid; 95% confidence level; 2,000 bootstrap resampling) using *selected events* from 4 June 1998 to 31 December 1999 (Figure 7). These resolved *TWs* are *TWA—4 June–13 August 1998; TWB—13 August–13 November 1998; TWC—13 November 1998–13 January 1999; TWD—13 January–31 December 1999*. We conclude the analysis for *TWs 2–7* and *TWs A–D* with Figure 7 and Table S4 in Supporting Information S1 to compare the corresponding grid-wise SHmax, σ_3 orientations. *R*-mean values, are listed in Figures 5 and 6 and Table S3 in Supporting Information S1.

3. Results

3.1. Rake-Analysis and Focal Mechanism Classification

Rake-based classification of selected events over all *TWs* show oscillations between oblique-normal and strike-slip faulting (Figures 3 and 4 and Figures S4–S6 in Supporting Information S1). In *TW1* oblique-normal events are dominant over strike-slip, while all other mechanisms seem subdued (Figure S4a in Supporting Information S1). In *TW2* (Figure 3a; Figure S5a in Supporting Information S1) Plane-a shows large numbers of left-lateral strike-slip (LLSS) and oblique-normal left-lateral strike-slip (ONLLSS) events (details in Table S2 of the Supporting Information S1). Meanwhile, Plane-b indicates prominence of oblique-normal right-lateral strike-slip (ONRLSS) over all other faulting styles. In *TW3* (Figure 3b; Figure S5b in Supporting Information S1), strike-slip and oblique-normal events are still dominant, although there is a higher ratio of oblique-normal to strike-slip events compared to *TW2*. Meanwhile, *TW4* (Figure 3c; Figure S5c in Supporting Information S1) exhibits a shift in the dominant faulting mechanism where the number of strike-slip events overshoots that of oblique-normal earthquakes. This trend continues in *TW5* (Figure 4a; Figure S6a in Supporting Information S1) where the ratio of strike-slip to oblique-normal events remains over unity. In *TW6* (Figure 4b; Figure S6b in Supporting Information S1), the trend reverses to a higher ratio of oblique-normal to strike-slip faulting earthquakes as observed previously in *TW2* and *TW3*; a trend that continues in *TW7* (Figure 4c; Figure S6c in Supporting Information S1). The ternary plots in Figures 3 and 4 further illustrate the magnitude- and depth- distributions of these events in each *TW*. In *TWs 2–3*, the depths are randomly distributed from 4 to 10 km-depth range, with the larger events occurring between 4 and 6 km-depth. The main distribution alters to 5.5 to 7 km-depth in *TWs 4–5*, but the relatively larger earthquakes occur between 4.5 and 6 km-depth. In *TW6*, events span the entire 4 to 10 km-depth, with the larger events (M_L 2 to 4) lying within 4 to 6 km-depth, although a larger proportion of the total events lie between 6 and 10 km-depth compared to the earlier *TWs*. The entire volume within 4 to 10 km-depth lights up in *TW7* as an aftermath of the 13 November 1998 mainshock. The plots comparing the strike- and rake-angles of the selected events are shown in Supporting Information S1 (Figure S8). *TWs* that host an abundance of nodal planes with strike-angles 0° ± 15° or 180° ± 15° accommodate right-lateral strike-slip (RLSS) and ONRLSS movement. The number of oblique-reverse right lateral strike-slip (ORRLSS) faulting planes seems to be very low. Meanwhile, most of the LLSS and ONLLSS motions are confined to strike angles of nodal planes oriented in the ~ENE or ~WSW direction (75° ± 15° or 255° ± 15°). This agrees with the general premise of seismic activity and plate motion directions in the Hjalli-Ölfus region.

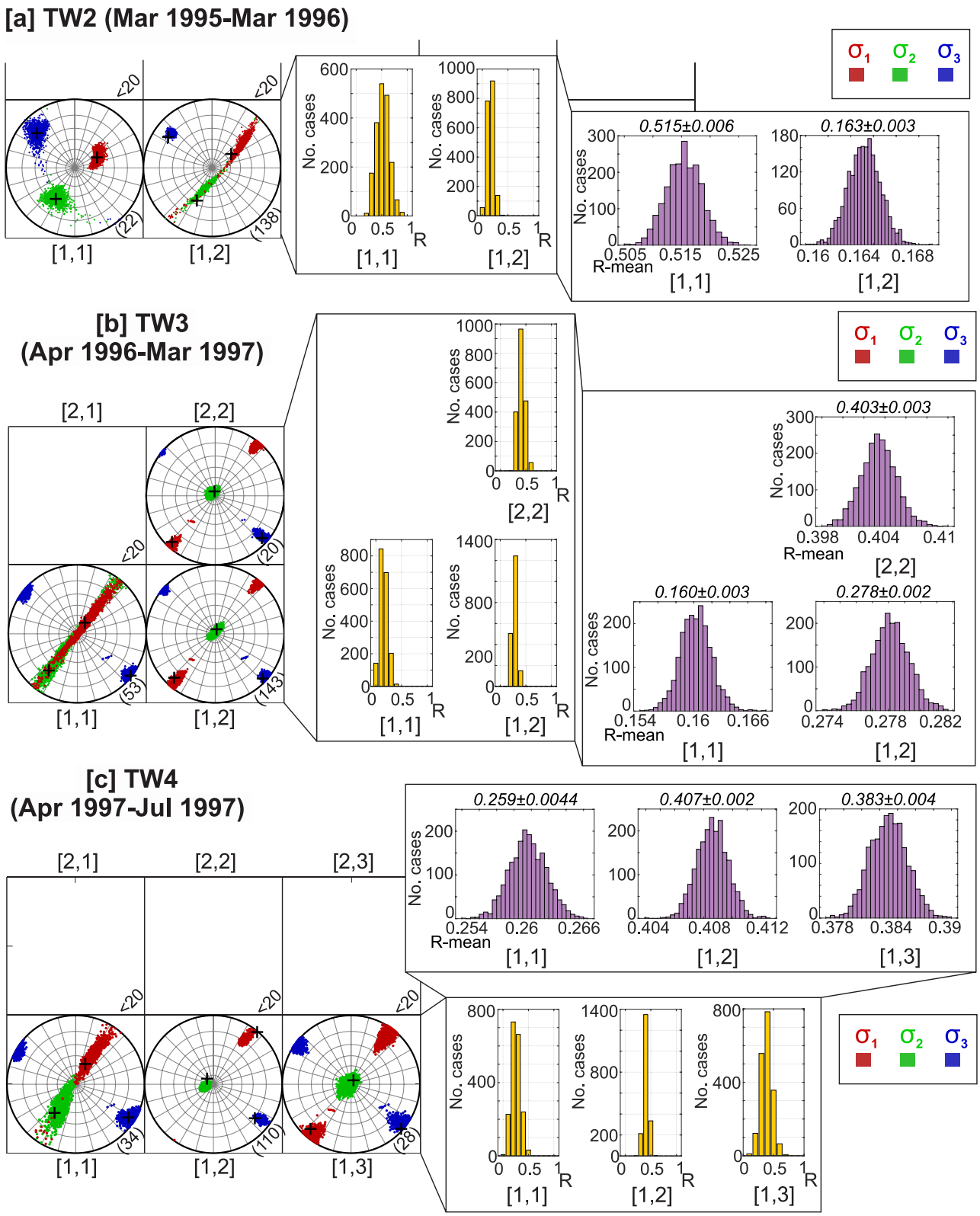
[a] TW2 (Mar 1995-Mar 1996)
[b] TW3 (Apr 1996-Mar 1997)
[c] TW4 (Apr 1997-Jul 1997)
σ1 σ2 σ3
No. cases
R
R-mean
0.515±0.006
0.163±0.003
0.403±0.003
0.160±0.003
0.278±0.002
0.259±0.0044
0.407±0.002
0.383±0.004
[1,1]
[1,2]
[1,3]
[2,1]
[2,2]
[2,3]

Figure 5.

It is not surprising that there is a lack of normal faulting events for strike angles of *selected events* since they align with the transform zone (Figures 3 and 4). Rake analysis of *non-selected events* also illustrate relatively low normal faulting in Hjalli-Ölfus during the study period. The exception is *TW2*, when normal faulting is the second dominant faulting style after oblique-normal events (Figure S7 in Supporting Information S1). In other *TWs*, FPSs of *non-selected events* mostly display the same characteristics as *selected events*, that is, strike-slip or oblique-normal faulting (Figure S7 in Supporting Information S1).

3.2. Spatio-Temporal Evolution of Stresses in Ölfus (1991–1999)

The stress-orientations and the distributions of R-values, for stress inversion using all events (Figures S10 and S11 in Supporting Information S1) are comparable to those using *selected events* (Figures 5 and 6), although more grids fulfill the minimum data requirement (20 events per grid: minimum number of polarities and amplitudes etc.) when all earthquakes are considered. Choosing all relocated events increases the ambiguity in the direction of the faulting planes (N-S, ENE-WSW, or other orientations) (Figures S10 and S11 in Supporting Information S1). Therefore, we choose to focus on the results from the inversion of *selected events* with nodal planes in line (±15°) with the dominant seismic trends in Hjalli-Ölfus (Figures 5 and 6).

In *TW2* (March 1995–March 1996), *R*-mean values in grids [1,1] and [1,2] are 0.515 ± 0.006 and 0.163 ± 0.003, respectively, with 95% confidence intervals for the standard error of the mean. This indicates that σ_1 is closer in magnitude to σ_2 in grid [1,2] than in grid [1,1], if the magnitude of σ_3 remains comparable across grids. In both active grids, σ_3 is near-horizontal although with a greater plunge than in most of the following TWs, while σ_1 and σ_2 are at significant plunges from the horizontal (Figure 5a). However, it is to be noted that the uncertainties for σ_1 and σ_2 in grid [1,2] are larger and overlap one another compared to grid [1,1], indicating that σ_1 and σ_2 are potentially interchangable. The stress field indicates oblique-normal faulting in grid [1,1] and a mixture of oblique-normal and strike-slip faulting in grid [1,2] (Figure 3a). In August 1994, there was a sudden surge of seismic moment release in Hengill (Feigl et al., 2000; Sigmundsson et al., 1997), which is moderately reflected in Hjalli-Ölfus (Figure 2b). However, the response of Hjalli-Ölfus to the Hengill swarm was more pronounced 1½ year later (*TW3*), concomitant with the inflation in Hengill observed by Feigl et al. (2000). Although *TW1* (July 1991–February 1995) has fewer *selected events*, the results for grids [1,1] and [1,2] are comparable to those in *TW2*, but with larger uncertainties (Figure 5 and Figure S9 in Supporting Information S1). Seismicity in *TW1* (July 1991–February 1995) is diffused but some lineaments can be traced in a N to N45°E and even E-W direction, unlike the predominant ∼N75°E trend in Hjalli-Ölfus in *TW2* and following *TWs* (Figure S1 in Supporting Information S1).

In *TW3* (April 1996–March 1997) the *R*-mean values of the three active grids [1,1], [1,2], [2,2] are 0.16 ± 0.003, 0.278 ± 0.002, 0.403 ± 0.003, respectively, indicating that the differences between the magnitudes of the principal stress axes σ_1 and σ_2 are low to moderate, assuming constant σ_3 magnitude across grids. σ_3 continues to be horizontal with comparable trends in grids [1,1], [1,2], and [2,2] (Table S4 in Supporting Information S1). In fact, σ_3 is horizontal or near-horizontal for the remaining *TWs*, and σ_1 is near-horizontal in grids [1,2] and [2,2]. However, in grid [1,1] the plunge angle distributions of σ_1 and σ_2 have overlapping confidence intervals, indicating comparable magnitudes and low *R*-mean values (Figure 5b). This change in the relative magnitude of σ_1 and σ_2 in grid [1,1] from *TW2* can be interpreted as an increase in magnitude of SHmax. In other words, SHmax in Hjalli-Ölfus was possibly increasing with the steady inflation in Hengill from 1993 with a growing stress gradient toward Hengill (i.e., highest *R*-mean value in grid [2,2]). *TW2* and *TW3* have the highest proportion of normal/oblique-normal to other faulting events compared to other well constrained *TWs*, both along prominent seismic trends and otherwise (Figures 3a and 3b; Figures S5a, S5b, S7a, and S7b in Supporting Information S1).

In *TW4* (April 1997–July 1997), active grids show similar horizontal σ_3 trends (Figure 5c). The near-horizontal to oblique orientation of σ_1 in grid [1,1] overlaps less with the σ_2 confidence intervals than before, suggesting an increase in σ_1 which is also reflected in an increased *R*-mean value in this grid. In grids [1,2] and [1,3], the trends

Figure 5. Grid-wise stress inversions for *TWs 2–4*. Selected events are inverted to estimate principal stress directions and corresponding *R*-distributions in individual grids over the following *TWs*. (a) *TW2*—March 1995–March 1996, (b) *TW3*—April 1996–March 1997, and (c) *TW4*—April 1997–July 1997. RGB-colored collection of bootstrap sampled inversions indicates 95% confidence intervals for the principal stress-axes ($\sigma_1, \sigma_2, \sigma_3$). Best-fit directions for the principal stress-axes are indicated by a "+" sign in corresponding clusters. *R*-value distributions for the respective grids are depicted using yellow bar-diagrams. Lavender bar diagrams illustrate bootstrapped *R*-mean (italics) and associated uncertainties of the computed *R*-values with 95% confidence intervals of the standard error of the mean. The numbers at the bottom right of each grid indicate the number of earthquakes in the grid. Grids with <20 earthquakes are not inverted.

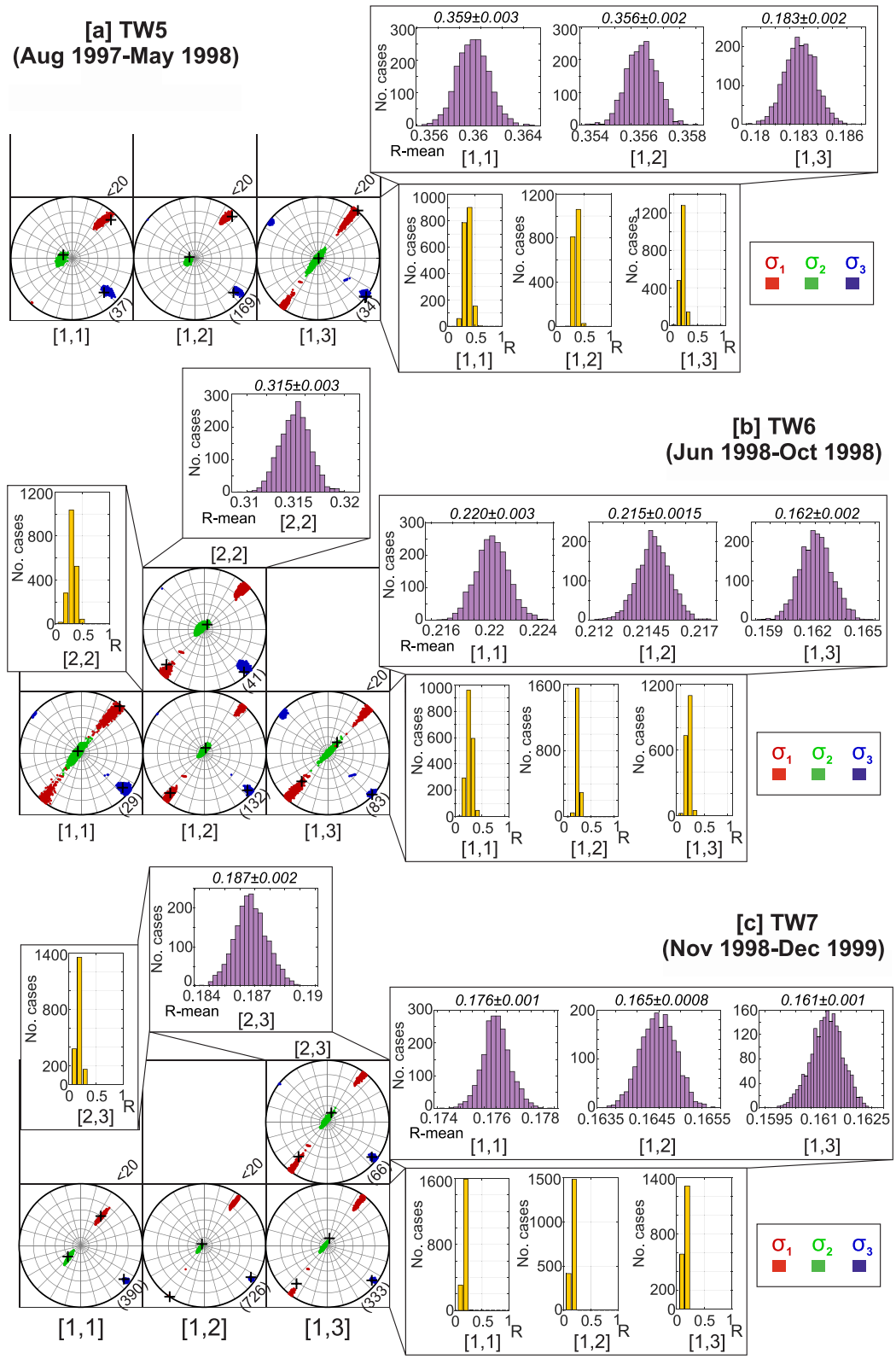

Figure 6. Grid-wise stress inversions for *TWs 5–7*. Selected events are inverted to estimate principal stress directions and corresponding *R*-distributions in individual grids over the following *TWs*. (a) *TW5*—August 1997–May 1998, (b) *TW6*—June 1998–October 1998, and (c) *TW7*—November 1998–December 1999. Bar diagrams, "+" sign, and RGB color descriptions as in Figure 5. The numbers at the bottom right of each grid indicate the number of earthquakes in the grid.

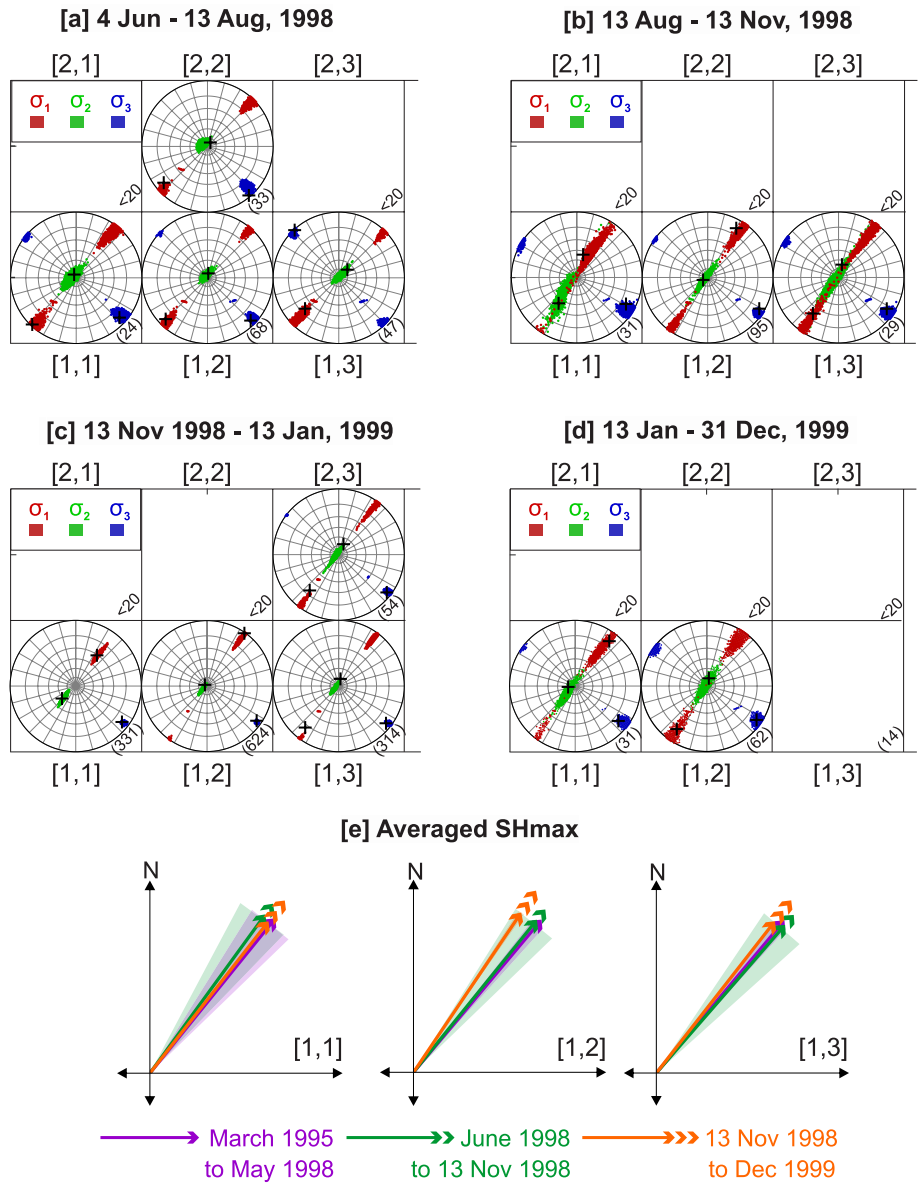

Figure 7. Stress inversion for selected events in resolved *TWs* (a) *TWA*—0000 hr, 4 June to 1038 hr, 13 August 1998, (b) *TWB*—1038 hr, 13 August to 1038 hr, 13 November 1998, (c) *TWC*—1038 hr, 13 November 1998 to 1038 hr, 13 January 1999, and (d) *TWD*—1038 hr, 13 January–31 December 1999. Hjalli-Ölfus Mw 5.1 occurred at 1038 hrs UTC on 13 November 1998. The numbers at the right bottom of each grid indicate the number of earthquakes in the grid. (e) Averaged SHmax with 95% confidence intervals for grids [1,1], [1,2], and [1,3].

of σ_1, σ_3 are near-horizontal with comparable orientations (Figure 5c; Table S4 in Supporting Information S1). The *R*-mean values in the three grids are 0.259 ± 0.004 [1,1], 0.407 ± 0.002 [1,2], 0.383 ± 0.004 [1,3], showing significant increase from *TW3* in grids [1,1] and [1,2]. The *R*-mean value of grid [1,3] is within the same range as the others and is comparable to its value in the previous *TW*. The *R*-mean value in grid [1,1] is low enough to prompt oblique-normal faulting. The directions of principal stresses in grid [1,2] are comparable in *TW3* and *TW4*. If the magnitudes of σ_2 and σ_3 do not change significantly between these time windows, the increase in the *R*-mean value can be interpreted as an increase in SHmax, due to the increased magnitude of the near horizontal σ_1 (Figures 5b and 5c). Seismicity in *TW4* delineates almost perfectly along the ~N75°E direction (Figure S1d in Supporting Information S1) and strike-slip faulting becomes the dominant mode over oblique-normal faulting (*TW2*, *TW3*) (Figure 3). Normal faulting events now account for 1%–2% of events in TW4 compared to the 5%–20% of events in prior *TWs* (Figure 3). Contemporary activity during April 1997 in Hengill shows a

continued increase in seismic moment release (Feigl et al., 2000), implying that Hengill inflation contributes to increased SHmax in Hjalli-Ölfus.

The grids active in *TW4* continue to remain so in *TW5* (August 1997–May 1998) with σ_1, σ_3 orientations near-horizontal (strike-slip) in all active grids (Figure 6a). The σ_3 trend falls within comparable range for most *TWs*. The SHmax and σ_3 directions are better constrained than in previous windows, with the SHmax directions in the range N39°E–N46°E (Figure 6a; Table S4 in Supporting Information S1). SHmax and σ_3 show apparent, but statistically insignificant, clockwise rotation in grids [1,1] and [1,2] between *TW4–5* (Figures 5c and 6a; Table S4 in Supporting Information S1). The R-mean values are 0.359 ± 0.003 [1,1], 0.356 ± 0.002 [1,2], 0.183 ± 0.002 [1,3], with a slight decrease in grid [1,2], a significant increase in grid [1,1], and a significant decrease in grid [1,3] compared to previous values in *TW4*.

In *TW6*, (June 1998–October 1998) there was a co- and postseismic increase in the ~ENE-WSW Hjalli-Ölfus seismicity following the June 1998 Hengill earthquake, and N-S trending shallow seismicity from Hengill in grid [2,2] that stopped at the Ölfus belt (Figure S1f in Supporting Information S1). The dominant faulting pattern shifted from strike-slip to oblique-normal, strike-slip being a close second. This is contrary to the two preceding *TWs*, where strike-slip was dominant (Figure 4; Figures S6b and S7e in Supporting Information S1). This change is reflected in the stress field in grids [1,1] and [1,3], where σ_1 is no longer near-horizontal (Figure 6b; Figure S12 in Supporting Information S1). Grid [2,2] becomes seismically active again (Figure 6b). The stress field in grids [1,2] and [2,2] show near horizontal σ_1, σ_3 trends (at 95% confidence level), while grids [1,1] and [1,3] show strike-slip to oblique-normal inducing stress. σ_3 is near-horizontal with comparable strike in all three southern grids and without significant change from *TW5* (Figures 6a and 6b; Table S4 in Supporting Information S1). The trend of σ_3 in grid [2,2] is not significantly different from the trends in the southern grids nor is there any significant change observed between *TW3* and *TW6*. The *R*-mean values 0.220 ± 0.003 [1,1], 0.215 ± 0.002 [1,2], and 0.162 ± 0.002 [1,3] indicate comparable principal stress magnitudes, while grid [2,2] with *R*-mean = 0.315 ± 0.003 indicates higher magnitude σ_1, lower σ_2 or both, assuming comparable σ_3 across grids. Lower magnitude σ_2 in grid [2,2] compared to the other grids could be due to shallower seismicity and by inference lower overburden pressure values. There is a significant decrease in *R*-mean of the southern grids between *TW5* and *TW6*, and between *TW3* and *TW6* for grid [2,2].

In *TW7* (November 1998–December 1999), the active grids are [1,1], [1,2], [1,3], and [2,3], all with low *R*-mean values 0.176 ± 0.001, 0.165 ± 0.001, 0.161 ± 0.001, and 0.187 ± 0.002, respectively (Figure 6c). As in *TW6*, the *TW7 R*-mean values in grids [1,1], [1,2], and [1,3] are low, but with a slight decrease compared to those in *TW6* in grids [1,1] and [1,2], and no significant change in [1,3]. Grid [2,3] has low R-mean values similar to those in the southern grids. Grids [1,2], [1,3], and [2,3] show near-horizontal σ_1, σ_3 confidence intervals, whereas [1,1] exhibits near-horizontal σ_3, and oblique σ_1. This is a change from *TW6*, where σ_1 ranged from a horizontal to an oblique plunge in grid [1,1]. Grid [2,3] is the site of the 14 November 1998 (mb = 4.7 and Ms = 4.1) Hjalli-Ölfus aftershock (ISC Bulletin, 2021), located on a N-S fault. The σ_3 trends in grids [1,1], [1,3], and [2,3] are similar. In all the southern grids that constitute the major trend of the Hjalli-Ölfus belt, and high aftershock activity, the stress field shows a counterclockwise rotation in *TW7*. The largest rotation is observed in grid [1,2] with SHmax now in direction 34° and σ_3 trending 124° compared to the mean values of 39° and 129° over all other *TWs* (Figures 6b and 6c; Table S4 in Supporting Information S1).

A closer look at *TW6* and *TW7* resolves the activity surrounding the 4 June 1998 Hengill mainshock and the 13 November 1998 Hjalli-Ölfus mainshock into 4 subdivisions. *TWA* (4 June—1038 hr, 13 August 1998) spans the co- and early post-seismic period of the 4 June 1998 Hengill (Mw = 5.4) earthquake. The stress inversion shows near-horizontal σ_1, σ_3 strike-slip faulting in all active grids with slightly more oblique solutions of σ_1 in grids [1,1] and [1,3] (Figure 7a). Grids [1,2] and [2,2] lie south of the Hengill mainshock (Parameswaran et al., 2020), which may explain the pronounced strike-slip activity in these grids. There is a significant reduction in the R-mean values between *TW5* and *TWA* in grids [1,1], [1,2], and a borderline statistically significant (change is greater than the associated uncertainty) increase in [1,3]. The apparent clockwise rotations of SHmax and σ_3 between *TW5* and *TWA* in grids [1,2] and [1,3] are not statistically significant although borderline significant in grid [1,3] (Figures 6a and 7a; Table S4 in Supporting Information S1). TWB (1,038 hr, 13 August–1,038 hr, 13 November 1998) consists of the Hengill (Mw = 5.4) aftershocks and the foreshocks of the 13 November 1998 Hjalli-Ölfus mainshock (Mw = 5.1). A considerable change is observed in the stress field from TWA to TWB. At 95% confidence level, σ_3 is horizontal as before, but σ_1 in grids [1,2] and [1,3] shows obliqueness, while a more

characteristic obliqueness is observed in grid [1,1]. The *R*-mean value in grid [1,2] is significantly reduced in *TWB*, slightly reduced in [1,1] and not significantly changed in [1,3] (Table S3 in Supporting Information S1). Lund and Bödvarsson (2002) reported an increase in solitary events (i.e., events with dissimilar spectral amplitudes, due to greater variety of focal mechanisms and/or spatial separation) starting in August in *TWB* until the Hjalli-Ölfus mainshocks, when the earthquake characteristics became similar again. Related to their observed dissimilarity, perhaps it is the wide range of σ_1 orientations in all three southern grids compared to *TWA* and *TW5* that sets *TWB* apart. *TWC* (1038 hr, 13 November 1998–1038 hr, 13 January 1999) spans the co-seismic and immediate aftershock sequence of the Hjalli-Ölfus mainshock. In *TWC* the trend of σ_3 is well constrained in horizontal position in all resolved grids. In grid [1,1] σ_1 is well constrained in an oblique position, and in [1,2] and [1,3] it is well constrained in a horizontal position. Grid [2,3] has a confidence interval of σ_1, ranging from horizontal to oblique. The *R*-mean value drops in grids [1,1] and [1,3], but increases slightly in gird [1,2] (Table S3 in Supporting Information S1). A statistically significant change in SHmax and σ_3 orientations between *TWB* and *TWC* is not observed (Table S4 in Supporting Information S1). *TWD* (1038 hr, 13 January–31 December 1999) spans the extended aftershocks of the Hjalli-Ölfus mainshock and the subsequent interseismic period. Only grids [1,1] and [1,2] are constrained in this period, with very similar stress characteristics between them. The stress field reverts to a state similar to that of *TWB*, where the confidence interval of σ_1 ranges from horizontal to oblique. There is no significant change in the σ_3 trend in *TWD* (Figure 7; Table S4 in Supporting Information S1). In *TWD*, the *R*-mean values in grids [1,1] and [1,2] begin to increase again, although they are still rather low, 0.195 ± 0.003 and 0.211 ± 0.003, respectively (Figure 7; Table S3 in Supporting Information S1). Therefore, both longer and shorter *TWs* show altering stress states in the prescribed grids over time and are discussed further in the following section.

4. Discussion

4.1. Current Understanding of Regional and Local Stress Fields in the SISZ

One of the early studies based on 605 earthquakes recorded by the SIL network in the SISZ ($0 < M_L \leq 2$) between July 1991 and February 1992, pointed to the maximum horizontal compressive stress (SHmax) trending ~N50°E (Stefánsson et al., 1993). Bjarnason, Cowie, et al. (1993) and Bjarnason, Menke, et al. (1993) measured a mean trend N40°E of tension fractures in the surface rupture of the 1912 magnitude 7.0 earthquake in the eastern end of the SISZ, which individually align with the maximum horizontal stress (Scholz, 2019). Analyzing paleo-stresses in rocks aging 3.1–0.7 Ma and employing 50 focal mechanisms from 1991 to 1995 in central parts of the SISZ, Bergerat et al. (1998) concluded that the dominant time-averaged regional stress field here has its maximum horizontal compressive stress oriented in the NNE-SSW to NE-SW direction, agreeing with the results from Stefánsson et al. (1993), Bjarnason, Cowie, et al. (1993), and Bjarnason, Menke, et al. (1993). They also conclude that there exists a contrasting stress field that has its maximum horizontal compressive stress trending NW-SE, which may be related to multiple factors such as stress release and rebound, and dike injections in nearby rift segments over time. A subsequent study by Bergerat et al. (1999) observes that, of the identified faults in the SISZ, half are normal faults, and the remaining are strike-slip, with no reverse faults observed in the field, reflecting both its past behavior, when it was part of the rift, and its present as a transform zone. They further note that 71% of earthquakes have strike-slip, 16% normal, and 13% reverse focal mechanisms in SISZ during present times, consistent with the net left-lateral motion of SISZ (Bergerat & Angelier, 2000; Bergerat et al., 1999). Stress field computations using borehole data from the western SISZ also point to ~NNE to NE trending SHmax, consistent with the large earthquakes in SISZ (Ziegler et al., 2016). Bergerat and Angelier. (2008) identify SISZ as a wide diffused transform area with predominantly ~N10°E right-lateral faults, some N70°E left-lateral faults, and no significant through-going E-W fault. Angelier et al. (2008) correlate these to a primary stress regime with a ~N45°E oriented compression and ~N135°E extension.

On a more local scale, Bergerat et al. (2003), who analyzed the right-lateral motion on the Leirubakki fault, ~3.5 km west of the surface rupture in Selsund following the 1912 M_S 7.0 earthquake in eastern SISZ (Kárník, 1969; Appendix B in Bjarnason, Cowie, et al., 1993; Bjarnason, Menke, et al., 1993), tentatively propose that the lack of clear ~E-W faulting along the SISZ might be a result of slip accommodation in a young and hot lithosphere with potential for discrete brittle left-lateral faults in a future, more mature state of the SISZ, as suggested by Einarsson and Eiríksson (1982), Bjarnason, Cowie, et al. (1993), and Bjarnason, Menke, et al. (1993). The Leirubakki fault, that lies 18 and 36 km east of the 17 and 21 June 2000 earthquakes, respectively, experienced lower postseismic

friction than pre-seismic friction, indicating change in stress field following the 2,000 earthquakes (Plateaux et al., 2010). This study also showed that the Skard fault, that lies 8 km west of the Leirubakki fault, shows contrasting changes in stress orientation compared to the latter. This change within fault structures, compared to regional stresses, is attributed to fluid flow within these structures and/or heterogeneities in their mechanical/hydraulic properties (e.g., Cappa, 2009; Gudmundsson et al., 2010).

Meanwhile, in western SISZ, a stress-inversion study using events between April 1998 and November 1998, before the mainshock on 13 November in Ölfus, shows the maximum horizontal stress oriented at ∼N30°E and the minimum horizontal stress trending ∼N60°W (Lund & Slunga, 1999). Lund and Bödvarsson (2002), who later performed stress inversions on earthquakes from 1 November 1997 to the 13 November 1998 Mw 5.1 earthquake, showed the disappearance of seismic self-similarity around August 1998 and its reappearance shortly after the mainshock. Hensch et al. (2016) conducted stress inversions using aftershocks of the 2008 ∼M6 Ölfus earthquakes, east of the Hjalli-Ölfus region, and found that SHmax orientations in Hjalli-Ölfus showed a counterclockwise rotation (36° ± 8° to 35° ± 8°) over the first month, followed by clockwise rotation (35° ± 8° to 40° ± 6°). A more recent study conducted using GPS data from 2001 to 2015 in SISZ to understand the pre-seismic strain anomalies before the 2008 ∼M6 earthquakes in Ölfus also points to a varying stress field in the region (Árnadóttir et al., 2018). The authors find that GPS horizontal velocities in the Ölfus region after the 29 May 2008 mainshock are larger and more northerly directed than before (counterclockwise rotation), and that they gradually rotate eastward (clockwise rotation) with decreasing magnitudes over the course of time (Árnadóttir et al., 2018). In the following sections we discuss the spatial and temporal evolution of stresses as manifested in focal mechanisms and principal stress axes orientations from July 1991 to December 1999 over *TWs* prescribed in this study.

4.2. Stress Evolution in the Hjalli-Ölfus Area Between March 1995 and December 1999

The average trend of SHmax and σ_3 for all grids from *TWs 2–7* is 40° ± 1° and 130° ± 1°, respectively. These trends are very similar to the inferred SHmax from rift structures in the eastern RP, which is significantly different from the geological trends of the Hengill volcanic zone (Sæmundsson et al., 2016). These values are also comparable to the regional trends obtained by a previous study in the Hjalli-Ölfus area (Hensch et al., 2016). Over *TWs 2–7* and *A–D*, grids [1,1], [1,2], and [1,3] have remained most consistently active. The mean SHmax orientations in these southern grids between March 1995 and December 1999 (*TWs 2–7*) are 39° ± 4°, 39° ± 2°, and 40° ± 2°, respectively (Figure 7; Table S4 and Figure S12 in Supporting Information S1). The mean SHmax orientations in the aforementioned southern grids from March 1995 to May 1998 (*TW2–5*), before the Hengill and the Hjalli-Ölfus earthquakes are 39° ± 7°, 40° ± 2°; 40° ± 2° respectively. After the Hengill event (4 June 1998), from June 1998 to 13 November 1998 (averaged *TW6* and *TWA–B*) the SHmax for these grids are 36° ± 8°, 39° ± 7°, 41 ± 7° respectively (Figure 7; Table S4; Figure S12 in Supporting Information S1). Following the Hjalli-Ölfus earthquake (13 November 1998), the SHmax orientations in the three grids are 38° ± 1°, 34° ± 1°; 38° ± 1° (Table S4 in Supporting Information S1). A significant counterclockwise rotation in SHmax orientation is therefore observed in grid [1,2] in *TW7* that includes the Hjalli-Ölfus mainshock compared to its mean value in the previous periods that is, *TW2–TW5* (Table S4 in Supporting Information S1). The larger uncertainties in the SHmax values in *TW6* and *TWA–B* could be due to the fact that these TWs include earthquakes from the NS fault extending southward from the Hengill system.

The five phases of stress evolution observed in Hjalli-Ölfus are as follows:

1. The initial state of stress in *TW2* (March 1995–;March 1996) is oblique-normal to strike-slip, with σ_3 trending ∼130° and corresponding average SHmax ∼40° (Figure 5a). In grid [1,1] σ_1 is oblique to near vertical (SHmax $\geq \sigma_2$), while in grid [1,2] σ_1 is oblique to near-horizontal (SHmax $\leq \sigma_1$). This represents an increase in SHmax magnitude from west to east. Time window *TW1* (July 1991–February 1995) spans a period mostly prior to the inflation in Hengill (Figure 2b). Although the stress field is less constrained in *TW1* than in *TW2*, the similarity in *R*-mean values and general orientations of the principal stresses (Figure S9 in Supporting Information S1) suggests a similar state of stress in these windows. These inferences of relative stress magnitudes and trends of SHmax and σ_3 suggest that the transtensional stress field of the RP extended into the Hjalli-Ölfus area, prior to and ∼1.5 year into the main period of unrest in the Hengill volcanic system. The interseismic state of stress in the Hjalli-Ölfus seems to be transtensional.
2. In *TW3* (April 1996–March 1997) a clear change in the stress field is observed; most likely related to the continued inflation in the Hengill volcanic zone. SHmax and σ_3 trends remain largely unchanged from the previous *TW*. However, altered *R*-mean values in the southern grids can be interpreted as an increase in

horizontal stress. Again, increased magnitude of SHmax from west to east can be observed, but also an increase to the north (grid [2,2]), in the direction of Hengill. From *TW1* through *TW3*, the state of stress in Hjalli-Ölfus seems to change from transtensional, like the RP, to a transform-faulting regime, like the SISZ.

3. In time windows *TW4 and TW5* (April 1997–May 1998), the mean trend of SHmax and σ_3 are not significantly different from the previous windows. The increased *R*-mean values and the horizontal orientation of σ_1 in grids [1,1] and [1,2] in *TW5* indicate gradually increasing loading in both. The *R*-mean in grid [1,3] is similar to the values of the other grids in *TW4*, but drops to a lower level in *TW5*. Horizontal stress loading (SHmax) on the Hjalli-Ölfus faults seems to reach its maximum in these time windows, prior to the Hengill mainshock when the R-mean values are at their highest in a dominantly strike-slip environment in Hjalli-Ölfus.
4. In *TW6* (June 1998–October 1998), the co- and post-seismic *TW* of the Hengill mainshock and pre-seismic window of the Hjalli-Ölfus main event, the stress field tends to be more oblique-normal, especially in the latter half of the window (*TWB*). Significant reduction in the *R*-mean values of grids [1,1] and [1,2] and a moderate decrease in grid [1,3] are observed. Orientations of σ_3 and σ_2 are mostly unchanged and if we assume magnitudes comparable to prior *TWs*, then there must be a reduction in magnitude of σ_1 that causes the lowering of R-mean values. This implies that the stress-drop due to the Hengill mainshock extends to the Hjalli-Ölfus area. The averaged SHmax trends in [1,2] and [1,3] are relatively unchanged, while in [1,1] it shows a mild counterclockwise (toward north) rotation, compared to the those from March 1995 to May 1998 (Figure 7e; Table S4 in Supporting Information S1). The latter half of the time window (*TWB*) shows continued reduction of the *R*-mean values, although no new significant events were recorded. The continued stress-drop here can be explained by a potential gradual post-seismic response of the Hengill mainshock. Another possible cause would be an increase in pore pressure following the Hengill earthquake, as pore pressure and *R*-values are negatively correlated for $R < 0.6$ (Martínez-Garzóin et al., 2016). Increased pore pressure has been suggested before as an explanation for a greater variety of faulting observed in this *TW* (Lund and Bödvarsson, 2002). The hypothesized increase in pore pressure is quite significant as the *R*-mean value drops to its lowest value observed in this study; *R*-mean $= 0.144 \pm 0.002$ in grid [1,2], where the Hjalli-Ölfus mainshock (Mw = 5.1) occurred (Table S3 in Supporting Information S1).
5. In *TW7* (November 1998–December 1999), that is, co- and post-seismic windows of the Hjalli-Ölfus mainshock of November 1998, the R-mean values drop again in a mostly strike-slip stress environment. We interpret this reduction as a stress-drop with reduced σ_1 and shear stress on the Hjalli-Ölfus faults. It is noteworthy that the *R*-mean reduction is smaller in this window than in the previous one, implying a slightly greater stress-drop in the Hjalli-Ölfus area due to the Hengill main earthquake, an event of greater magnitude than the Hjalli-Ölfus November events. The averaged SHmax trends in grid [1,1] shows a mild clockwise rotation (toward east) unlike grids [1,2] and [1,3], where the rotation is counterclockwise (toward north) in this *TW* (Figure 7e; Table S4 in Supporting Information S1). In the central southern grid [1,2], at the location of the epicenter of the Hjalli-Ölfus mainshock, the horizontal stress components are now closer to the observed geological trends in the Hengill volcanic system (Table S4 in Supporting Information S1). The largest stress-drop may have occurred in the central southern grid. This *TW*, with respect to its predecessor, elucidates the variability of loading and stress-drop over time and spatial grids.

5. Conclusions

This study attempts to quantify the states of stress and earthquake focal mechanisms in the Hjalli-Ölfus region between July 1991 and December 1999. We find:

1. Inflation and seismic unrest of the Hengill volcanic system started in July 1994, but did not affect the Hjalli-Ölfus area until ~1–1½ years later. The main faulting characteristics until that time was oblique-normal faulting. The trend of horizontal stress in Hjalli-Ölfus is similar to that of its western neighbor, the eastern RP (inferred from geological structures), with SHmax $\sim 40° \pm 1°$ and near-horizontal $\sigma_3 \sim 130° \pm 1°$. Interseismic stress in Hjalli-Ölfus may therefore be more related to the transtentional stress of the RP than that of the SISZ transform zone or the Hengill volcanic zone.
2. The eventual loading of the Hjalli-Ölfus area due to the Hengill volcanic system was characterized by an incremental increase (averaged over time windows) in the magnitude of SHmax. The faulting characteristics in the area changed from the initial stage to near-equal parts oblique-normal/strike-slip, and then to a pure strike-slip regime when SHmax reached its peak. The western part of Hjalli-Ölfus, and closest to the RP, was the last to change to a strike-slip stress state. Under a strike-slip stress regime, the observed trends of

the principal horizontal stresses in Hjalli-Ölfus favor similar manners of slip on conjugate pairs of ~NS and ~ENE-WSW striking faults, both of which are observed in seismic lineations.

3. Maximum SHmax loading in Hjalli-Ölfus occurred before the June 1998 Mw = 5.4 Hengill mainshock. The epicenter of this mainshock was located on a ~NS strike-slip fault, ~10 km north of Hjalli-Ölfus. The stress-drop and aftershocks of the Hengill mainshock extended to the Hjalli-Ölfus area, and seemingly reduced the horizontal stresses here. The stress-drop seems to have been gradual over the post-seismic period of the Hengill earthquake (perhaps due to pore pressure), occurring prior to the November 1998 Hjalli-Ölfus mainshock (Mw = 5.1). The Hjalli-Ölfus mainshock added to the stress-drop on the Hjalli-Ölfus fault structures.
4. The combined unloading of stresses following the Hengill and the Hjalli-Ölfus mainshocks resulted in a counterclockwise rotation of ~5° (95% confidence level) of the maximum horizontal stress (SHmax) in the Hjalli-Ölfus area. The SHmax rotated counterclockwise toward ~N-S faults with respect to the main ~ENE-WSW (N75°E) striking seismic lineaments in the Hjalli-Ölfus aftershock period.
5. In a yearlong post-seismic period after the Hjalli-Ölfus mainshocks, the stress-state seems to return to initial conditions, that is, similar to state of stress in the RP, before the influence of the unrest near Hengill.

Through this study we illustrate the utility of measuring the rotation of maximum horizontal stress to estimate stress loading and unloading during tectonic events (deformation) in enhancing our understanding of earthquake mechanics, for example, earthquake triggering on neighboring faults over seismic and interseismic periods.

Data Availability Statement

The relocated earthquake catalogues, station lists, and seismic velocity model used have all been uploaded to the Open Science Framework website following the AGU FAIR-data policy (https://osf.io/a58fv/?view_only=02c75823f6c24da98ca6adbab5543567). The fault plane solutions were obtained directly from the Icelandic Meteorological Office (IMO), and are uploaded to the Open Science Framework website (https://osf.io/46kfr/?view_only=f61b8664d2c74b7d93819db24b300d4d). The project facilitated the procurement of seismic data recorded by the SIL seismic network from the IMO. Additional raw data can be obtained from the IMO. No new data has been generated in this study and the details of the uploaded data can be found in the Supplementary material of a previous publication https://doi.org/10.1029/2019JB019203.

Acknowledgments
This study was part of the project "4D seismic of the South Iceland Seismic Zone: Strong earthquake forecasting" (number 152432-053) funded by the Icelandic Research Fund (IRF) (Rannís) awarded to Ingi Th. Bjarnason (principal investigator). The authors would like to thank Thóra Árnadóttir for initial comments on this study and Ólafur Grímur Björnsson for editorial corrections. The authors also thank Gunnar B. Guðmundsson and Kristín Vogfjörð from the Icelandic Meteorological office (IMO) for sharing the seismic data, and Björn Lund (Uppsala University) for detailed comments and suggestions on this work.

References

Aki, K., & Richards, P. (1980). *Quantitative seismology, theory and methods* (Vol. I–II). W.H. Freeman.

Alvarez-Gomez, J. A. (2019). FMC-A one-liner python tool for earthquake focal mechanisms data management, cluster and classification. In *AGU Fall Meeting Abstracts* (Vol. 2019, pp. S11G–0431).

Angelier, J., Bergerat, F., Stefánsson, R., & Bellou, M. (2008). Seismotectonics of a newly formed transform zone near a hotspot: Earthquake mechanisms and regional stress in the South Iceland Seismic Zone. *Tectonophysics*, *447*(1–4), 95–116. https://doi.org/10.1016/j.tecto.2006.07.016

Árnadóttir, T., Geirsson, H., & Einarsson, P. (2004). Coseismic stress changes and crustal deformation on the Reykjanes Peninsula due to triggered earthquakes on 17 June 2000. *Journal of Geophysical Research*, *109*(B9), B09307. https://doi.org/10.1029/2004JB003130

Árnadóttir, T., Geirsson, H., & Jiang, W. (2008). Crustal deformation in Iceland: Plate spreading and earthquake deformation. *Jökull Journal*, *58*(1), 59–74. https://doi.org/10.33799/jokull2008.58.059

Árnadóttir, T., Haines, J., Geirsson, H., & Hreinsdóttir, S. (2018). A preseismic strain anomaly detected before M6 earthquakes in the South Iceland Seismic Zone from GPS station velocities. *Journal of Geophysical Research: Solid Earth*, *123*(12), 11–091. https://doi.org/10.1029/2018JB016068

Árnadóttir, T., Hreinsdóttir, S., Gudmundsson, G., Einarsson, P., Heinert, M., & Völksen, C. (2001). Crustal deformation measured by GPS in the South Iceland Seismic Zone due to two large earthquakes in June 2000. *Geophysical Research Letters*, *28*(21), 4031–4033. https://doi.org/10.1029/2001GL013332

Árnadóttir, T., Jiang, W., Feigl, K. L., Geirsson, H., & Sturkell, E. (2006). Kinematic models of plate boundary deformation in Southwest Iceland derived from GPS observations. *Journal of Geophysical Research*, *111*(B7), B07402. https://doi.org/10.1029/2005JB003907

Bergerat, F., & Angelier, J. (2000). The South Iceland Seismic Zone: Tectonic and seismotectonic analyses revealing the evolution from rifting to transform motion. *Journal of Geodynamics*, *29*(3–5), 211–231. https://doi.org/10.1016/S0264-3707(99)00046-0

Bergerat, F., & Angelier, J. (2008). Immature and mature transform zones near a hot spot: The South Iceland Seismic Zone and the Tjörnes Fracture Zone (Iceland). *Tectonophysics*, *447*(1–4), 142–154. https://doi.org/10.1016/j.tecto.2006.05.046

Bergerat, F., Angelier, J., Gudmundsson, Á., & Torfason, H. (2003). Push-ups, fracture patterns, and palaeoseismology of the Leirubakki Fault, South Iceland. *Journal of Structural Geology*, *25*(4), 591–609. https://doi.org/10.1016/S0191-8141(02)00051-2

Bergerat, F., Angelier, J., & Verrier, S. (1999). Tectonic stress regimes, rift extension and transform motion: The South Iceland Seismic Zone. *Geodynamica Acta*, *12*(5), 303–319. https://doi.org/10.1016/S0985-3111(00)87047-3

Bergerat, F., Gudmundsson, Á., Angelier, J., & Rögnvaldsson, S. T. (1998). Seismotectonics of the central part of the South Iceland Seismic Zone. *Tectonophysics*, *298*(4), 319–335. https://doi.org/10.1016/S0040-1951(98)00191-7

Bjarnason, I. T., Cowie, P., Anders, M. H., Seeber, L., & Scholz, C. H. (1993). The 1912 Iceland earthquake rupture: Growth and development of a nascent transform system. *Bulletin of the Seismological Society of America*, *83*(2), 416–435.

Bjarnason, I. T., Menke, W., Flóvenz, Ó. G., & Caress, D. (1993). Tomographic image of the mid-Atlantic plate boundary in south western Iceland. *Journal of Geophysical Research*, *98*(B4), 6607–6622. https://doi.org/10.1029/92JB02412

Björnsson, S. (1976). Earthquakes in Iceland (In Icelandic, with English abstract). *Náttúrufrædingurinn*, *45*(2), 110–133. https://hdl.handle.net/20.500.11815/1323

Bödvarsson, R., Rognvaldsson, S. T., Jakobsdottir, S. S., Slunga, R., & Stefánsson, R. (1996). The SIL data acquisition and monitoring system. *Seismological Research Letters*, *67*(5), 35–46. https://doi.org/10.1785/gssrl.67.5.35

Brandsdóttir, B., Parsons, M., White, R. S., Gudmundsson, Ó., Drew, J., & Thorbjarnardóttir, B. S. (2010). The May 29, 2008 earthquake aftershock sequence within the South Iceland Seismic Zone: Fault locations and source parameters of aftershocks. *Jökull: Journal of the Glaciological and Geological Societies of Iceland*, *60*(1), 23–46. https://doi.org/10.33799/jokull2010.60.023

Cappa, F. (2009). Modelling fluid transfer and slip in a fault zone when integrating heterogeneous hydromechanical characteristics in its internal structure. *Geophysical Journal International*, *178*(3), 1357–1362. https://doi.org/10.1111/j.1365-246x.2009.04291.x

Clifton, A. E., & Schlische, R. W. (2003). Fracture populations on the Reykjanes Peninsula, Iceland: Comparison with experimental clay models of oblique rifting. *Journal of Geophysical Research*, *108*(B2), 2074. https://doi.org/10.1029/2001JB000635

Ducrocq, C., Geirsson, H., Árnadóttir, T., Juncu, D., Drouin, V., Gunnarsson, G., et al. (2021). Inflation-deflation episodes in the Hengill and Hrómundartindur volcanic complexes, SW Iceland. *Frontiers of Earth Science*, *9*, 915. https://doi.org/10.3389/feart.2021.725109

Efron, B., & Tibshirani, R. (1986). Bootstrap methods for standard errors, confidence intervals, and other measures of statistical accuracy. *Statistical Science*, *1*(1), 54–75. https://doi.org/10.1214/ss/1177013815

Einarsson, P., Björnsson, S., Foulger, G. R., Stefánsson, R., & Skaftadóttir, T. (1981). Seismicity pattern in the South Iceland Seismic Zone. In D. Simpson & P. G. Richards (Eds.), *Earthquake prediction—An international review* (Vol. 4, pp. 141–151). American Geophysical Union Maurice Ewing Series.

Einarsson, P., & Eiríksson, J. (1982). Earthquake fractures in the districts land and Rangárvellir in the South Iceland Seismic Zone. *Jökull*, *32*(32), 113–120. https://doi.org/10.33799/jokull1982.32.113

Erlendsson, P., & Einarsson, P. (1996). The Hvalhnúkur Fault, a strike-slip fault mapped within the Reykjanes Peninsula oblique rift, Iceland. In B. Thorkelsson (Ed.), *Seismology in Europe* (pp. 498–504). European Seismological Commission.

Feigl, K. L., Gasperi, J., Sigmundsson, F., & Rigo, A. (2000). Crustal deformation near Hengill volcano, Iceland, 1993–1998: Coupling between magmatic activity and faulting inferred from elastic modeling of satellite radar interferograms. *Journal of Geophysical Research*, *105*(B11), 25655–25670. https://doi.org/10.1029/2000JB900209

Flóvenz, Ó. G., Wang, R., Hersir, G. P., Dahm, T., Hainzl, S., Vassileva, M., et al. (2022). Cyclical geothermal unrest as a precursor to Iceland's 2021 Fagradalsfjall eruption. *Nature Geoscience*, *15*(5), 397–404. https://doi.org/10.1038/s41561-022-00930-5

Geoffroy, L., & Dorbath, C. (2008). Deep downward fluid percolation driven by localized crust dilatation in Iceland. *Geophysical Research Letters*, *35*(17), L17302. https://doi.org/10.1029/2008GL034514

Gudmundsson, Á. (2007). Infrastructure and evolution of ocean-ridge discontinuities in Iceland. *Journal of Geodynamics*, *43*(1), 6–29. https://doi.org/10.1016/j.jog.2006.09.002

Gudmundsson, Á., Simmenes, T. H., Larsen, B., & Philipp, S. L. (2010). Effects of internal structure and local stresses on fracture propagation, deflection, and arrest in fault zones. *Journal of Structural Geology*, *32*(11), 1643–1655. https://doi.org/10.1016/j.jsg.2009.08.013

Hardebeck, J. L., & Michael, A. J. (2006). Damped regional-scale stress inversions: Methodology and examples for southern California and the Coalinga aftershock sequence. *Journal of Geophysical Research*, *111*(B11), B11310. https://doi.org/10.1029/2005JB004144

Hensch, M., Lund, B., Árnadóttir, T., & Brandsdóttir, B. (2016). Temporal stress changes associated with the 2008 May 29 MW 6 earthquake doublet in the western South Iceland Seismic Zone. *Geophysical Journal International*, *204*(1), 544–554. https://doi.org/10.1093/gji/ggv465

Hreinsdóttir, S., Árnadóttir, T., Decriem, J., Geirsson, H., Tryggvason, A., Bennett, R. A., & LaFemina, P. (2009). A complex earthquake sequence captured by the continuous GPS network in SW Iceland. *Geophysical Research Letters*, *36*(12), L12309. https://doi.org/10.1029/2009GL038391

Icelandic Meteorological Office (IMO). (2017). Preliminary analysed data by the SIL seismic monitoring group of the Icelandic Meteorological Office.

International Seismological Centre (ISC). (2021). On-line Bulletin. https://doi.org/10.31905/D808B830

Jakobsdóttir, S. S. (2008). Seismicity in Iceland: 1994–2007. *Jökull*, *58*(1), 75–100. https://doi.org/10.33799/jokull2008.58.075

Kárnir, V. (1969). *Seismicity of the European area 1*. Reidel.

Keiding, M., Árnadóttir, T., Sturkell, E., Geirsson, H., & Lund, B. (2008). Strain accumulation along an oblique plate boundary: The Reykjanes Peninsula, Southwest Iceland. *Geophysical Journal International*, *172*(2), 861–872. https://doi.org/10.1111/j.1365-246X.2007.03655.x

Keiding, M., Lund, B., & Árnadóttir, T. (2009). Earthquakes, stress and strain along an oblique divergent plate boundary: Reykjanes Peninsula, south-west Iceland. *Journal of Geophysical Research*, *114*(B9), B09306. https://doi.org/10.1029/2008JB006253

Khodayar, M., Björnsson, S., Gudnason, E. Á., Níelsson, S., Axelsson, G., & Hickson, C. (2018). Tectonic control of the Reykjanes geothermal field in the oblique rift of SW Iceland: From regional to reservoir scales. *Open Journal of Geology*, *8*(03), 333–382. https://doi.org/10.4236/ojg.2018.83021

Lund, B., & Bödvarsson, R. (2002). Correlation of microearthquake body-wave spectral amplitudes. *Bulletin of the Seismological Society of America*, *92*(6), 2419–2433. https://doi.org/10.1785/0119990156

Lund, B., & Slunga, R. (1999). Stress tensor inversion using detailed microearthquake information and stability constraints: Application to Ölfus in southwest Iceland. *Geophysical Research Letters*, *104*(B7), 14947–14964. https://doi.org/10.1029/1999jb900111

Lund, B., & Townend, J. (2007). Calculating horizontal stress orientations with full or partial knowledge of the tectonic stress tensor. *Geophysical Journal International*, *170*(3), 1328–1335. https://doi.org/10.1111/j.1365-246X.2007.03468.x

Martínez-Garzón, P., Kwiatek, G., Ickrath, M., & Bohnhoff, M. (2014). MSATSI: A MATLAB package for stress inversion combining solid classic methodology, a new simplified user-handling, and a visualization tool. *Seismological Research Letters*, *85*(4), 896–904. https://doi.org/10.1785/0220130189

Martínez-Garzón, P., Vavryčuk, V., Kwiatek, G., & Bohnhoff, M. (2016). Sensitivity of stress inversion of focal mechanisms to pore pressure changes. *Geophysical Research Letters*, *43*(16), 8441–8450. https://doi.org/10.1002/2016GL070145

Michael, A. J. (1984). Determination of stress from slip data: Faults and folds. *Journal of Geophysical Research*, *89*(B13), 11517–11526. https://doi.org/10.1029/JB089iB13p11517

Parameswaran, R. M., Thorbjarnardóttir, B. S., Stefánsson, R., & Bjarnason, I. T. (2020). Seismicity on conjugate faults in Ölfus, South Iceland: Case study of the 1998 Hjalli-Ölfus earthquake. *Journal of Geophysical Research: Solid Earth*, *125*(8), e2019JB019203. https://doi.org/10.1029/2019JB019203

Perlt, J., & Heinert, M. (2006). Kinematic model of the South Icelandic tectonic system. *Geophysical Journal International*, *164*(1), 168–175. https://doi.org/10.1111/j.1365-246X.2005.02795.x

Plateaux, R., Angelier, J., Bergerat, F., Cappa, F., & Stefánsson, R. (2010). Stress changes induced at neighboring faults by the June 2000 earthquakes, South Iceland Seismic Zone. *Terra Nova*, *22*(2), 79–86. https://doi.org/10.1111/j.1365-3121.2009.00919.x

Rickard, M. J. (1972). Fault classification: Discussion. *Geological Society of America Bulletin*, *83*(8), 2545–2546. https://doi.org/10.1130/0016-7606(1972)83[2545:fcd]2.0.co;2

Rögnvaldsson, S. T., Gudmundsson, G., Águstsson, K., Jakobsdóttir, S., Slunga, R., & Stefánsson, R. (1998). *Overview of the 1993-1996 seismicity near Hengill. Technical Report VI-R98006*. Icelandic Meteorological Office.

Rögnvaldsson, S. T., Arnadóttir, T., Agústsson, K., Skaftadóttir, T., Guðmundsson, G., Björnsson, G., et al. (1998). Skjálftahrina í Ölfusi í nóvember 1998. Technical Report.

Rögnvaldsson, S. T., & Slunga, R. (1993). Routine fault plane solutions for local networks: A test with synthetic data. *Bulletin of the Seismological Society of America*, *83*(4), 1232–1247. https://doi.org/10.1785/BSSA0830041232

Roth, F. (2004). Stress changes modelled for the sequence of strong earthquakes in the South Iceland Seismic Zone since 1706. In *Geodetic and geophysical effects associated with seismic and volcanic hazards (1305–1327)*. Birkhäuser. https://doi.org/10.1007/978-3-0348-7897-5_2

Sæmundsson, K., Magnús, Á., Sigurgeirsson, M. Á., Hjartarson, Á., Kaldal, I., Kristinsson, S. G., & Víkingsson, S., (2016). Geological map of Southwest Iceland, 1:100 000 (2. Eds.). *Iceland geosurvey*, Retrieved from https://arcgisserver.isor.is/

Scholz, C. H. (2019). *The mechanics of earthquakes and faulting*. Cambridge University Press.

Sigmundsson, F., Einarsson, P., Hjartardóttir, Á. R., Drouin, V., Jónsdóttir, K., Árnadóttir, T., et al. (2018). Geodynamics of Iceland and the signatures of plate spreading. *Journal of Volcanology and Geothermal Research*, *391*, 106436. https://doi.org/10.1016/j.jvolgeores.2018.08.014

Sigmundsson, F., Einarsson, P., Rögnvaldsson, S. T., Foulger, G. R., Hodgkinson, K. M., & Thorbergsson, G. (1997). The 1994–1995 seismicity and deformation at the Hengill triple junction, Iceland: Triggering of earthquakes by minor magma injection in a zone of horizontal shear stress. *Journal of Geophysical Research*, *102*(B7), 15151–15161. https://doi.org/10.1029/97JB00892

Slunga, R. (1981). Earthquake source mechanism determination by use of body-wave amplitudes—An application to Swedish earthquakes. *Bulletin of the Seismological Society of America*, *71*(1), 25–35. https://doi.org/10.1785/BSSA0710010025

Stefánsson, R. (2011). *Advances in earthquake prediction, research and risk mitigation* (p. 271). Springer-Verlag, Berlin and Heidelberg, in association with PRAXIS Publishing in UK.

Stefánsson, R., Bödvarsson, R., Slunga, R., Einarsson, P., Jakobsdottir, S., Bungum, H., et al. (1993). Earthquake prediction research in the South Iceland Seismic Zone and the SIL project. *Bulletin of the Seismological Society of America*, *83*, 696–716.

Stefánsson, R., Gudmundsson, G. B., & Halldórsson, P. (2000). *The two large earthquakes in the South Iceland Seismic Zone on June 17 and 21, 2000. Report VI-GOOOlO-JA04*. Icelandic Meteorology Office.

Vogfjörd, K. S., Hjaltadóttir, S., & Slunga, R. (2005). Volcano-tectonic interaction in the Hengill region, Iceland during 1993–1998. In *Geophysical research abstracts* (Vol. 7). European Geosciences Union.EGU05-J-09947.

Waite, G. P., & Smith, R. B. (2004). Seismotectonics and stress field of the Yellowstone volcanic plateau from earthquake first-motions and other indicators. *Journal of Geophysical Research*, *109*(B2), B02301. https://doi.org/10.1029/2003JB002675

White, B. J. P., Smith, R. B., Husen, S., Farrell, J. M., & Wong, I. (2009). Seismicity and earthquake hazard analysis of the Teton–Yellowstone region, Wyoming. *Journal of Volcanology and Geothermal Research*, *188*(1–3), 277–296. https://doi.org/10.1016/j.jvolgeores.2009.08.015

Ziegler, M., Rajabi, M., Heidbach, O., Hersir, G. P., Ágústsson, K., Árnadóttir, S., & Zang, A. (2016). The stress pattern of Iceland. *Tectonophysics*, *674*, 101–113. https://doi.org/10.1016/j.tecto.2016.02.008